



Article

Optimized Properties in Multifunctional Polyphenylene Sulfide Composites via Graphene Nanosheets/Boron Nitride Nanosheets Dual Segregated Structure under High Pressure

Liangqing Zhang ¹, Shugui Yang ², Longgui Peng ¹, Kepeng Zhong ³ and Yanhui Chen ^{3,*}

¹ College of Material Science and Engineering, Xi'an University of Science and Technology, Xi'an 710054, China

² Shaanxi International Research Center for Soft Matter, State Key Laboratory for Mechanical Behavior of Materials, Xi'an Jiaotong University, Xi'an 710049, China

³ School of Chemistry and Chemical Engineering, Shaanxi Key Laboratory of Macromolecular Science and Technology, Key Laboratory of Special Functional and Smart Polymer Materials, Ministry of Industry and Information Technology, Northwestern Polytechnical University, Xi'an 710072, China

* Correspondence: yanhuichen@nwpu.edu.cn; Tel.: +86-029-88431656



Citation: Zhang, L.; Yang, S.; Peng, L.; Zhong, K.; Chen, Y. Optimized Properties in Multifunctional Polyphenylene Sulfide Composites via Graphene Nanosheets/Boron Nitride Nanosheets Dual Segregated Structure under High Pressure. *Nanomaterials* **2022**, *12*, 3543. <https://doi.org/10.3390/nano12193543>

Academic Editor: Jean-Christophe P. Gabriel

Received: 30 August 2022

Accepted: 7 October 2022

Published: 10 October 2022

Publisher's Note: MDPI stays neutral with regard to jurisdictional claims in published maps and institutional affiliations.



Copyright: © 2022 by the authors. Licensee MDPI, Basel, Switzerland. This article is an open access article distributed under the terms and conditions of the Creative Commons Attribution (CC BY) license (<https://creativecommons.org/licenses/by/4.0/>).

Abstract: The practical application of polymer composites in the electronic and communications industries often requires multi-properties, such as high thermal conductivity (TC), efficient electromagnetic interference (EMI) shielding ability with low electrical conductivity, superior tribological performance, reliable thermal stability and excellent mechanical properties. However, the integration of these mutually exclusive properties is still a challenge, ascribed to their different requirement on the incorporated nanofillers, composite microstructure as well as processing process. Herein, a well-designed boron nitride nanosheet (BN)/graphene nanosheet (GNP)/polyphenylene sulfide (PPS) composite with a dual-segregated structure is fabricated via high-pressure molding. Rather than homogenous mixing of the hybrid fillers, GNP is first coated on PPS particles and followed by encapsulating the conductive GNP layers with insulating BN, forming a BN shell-GNP layer-PPS core composite particles. After hot-pressing, a dual segregated structure is constructed, in which GNP and BN are distinctly separated and arranged in the interfaces of PPS, which on the one hand gives rise to high thermal conductivity, and on the other hand, the aggregated BN layer can act as an “isolation belt” to effectively reduce the electronic transmission. Impressively, high-pressure is loaded and it has a more profound effect on the EMI shielding and thermal conductive properties of PPS composites with a segregated structure than that with homogenous mixed-structure composites. Intriguingly, the synergetic enhancement effect of BN and GNP on both thermal conductive performance and EMI shielding is stimulated by high pressure. Consequently, PPS composites with 30 wt% GNP and 10 wt% BN hot-pressed under 600 MPa present the most superior comprehensive properties with a high TC of 6.4 W/m/K, outstanding EMI SE as high as 70 dB, marvelous tribological performance, reliable thermal stability and satisfactory mechanical properties, which make it promising for application in miniaturized electronic devices in complex environments.

Keywords: boron nitride; graphene; polyphenylene sulfide; thermal conductive; electromagnetic interference shielding

1. Introduction

With electronic devices moving toward integration and miniaturization, the inevitability of overheating becomes a serious problem, which results in severe performance deterioration and service life decay of the electronic parts and components [1–3]. Along with heat emission, electromagnetic interference (EMI) pollution in modern wireless communication devices is also a problem which not only deteriorates the performance of electronic components but also endangers people's health [4–6]. Moreover, considering the complex

application environments of electronic gadgets, electrical insulation, thermal stability, wear resistance and mechanical properties are the prime requirements [7,8]. Therefore, it is attractive to fabricate polymer composites with the integration of these mutually exclusive multifunctional properties, which is meaningful for both the design philosophy itself and the form and capabilities of the products. However, the contradictions between the requirements of incorporated nanofillers, composite microstructure as well as the processing process aimed at different properties make the realization of multifunctionality still challenging. For example, the usage of functional nanofiller is essential in endowing composites with a sort of function, and normally an excess of it is incorporated in polymer composites to ensure a satisfying enhancement in this specific property, while this, in turn, inevitably degrades the inherent mechanical properties of the polymer matrix. Therefore, it is of great importance to ameliorate functional properties under low filler loading [9–11]. In pursuit of high-performance multifunctional polymer composites with low filler loading, structure optimization is an effective method. Up to now, extensive investigations into the structural design of polymer composites have been carried out [12]. For instance, sandwich structures [13,14], multilayered structures [15,16], porous structures [17,18], gradient structures [19], and segregated structures [20] were designed, aiming for the restricted distribution and favorable interconnection of functional fillers. Among which, the construction of segregated architecture with conductive fillers selectively located on the boundaries of polymer particles has been widely acknowledged to be an effective method to elevate the EMI shielding and thermal conductive performance.

Satisfactory EMI shielding of conductive polymer composites (CPC) can be obtained by the construction of a segregated architecture. Yan et al. reported a high-performance electromagnetic interference shielding reduced graphene oxide/polystyrene composite with a multi-facet segregated structure, which exhibits an optimized EMI SE of 45.1 dB [20]. Hu et al. fabricated a segregated polypropylene/ammonium polyphosphate/carbon nanotube (CNT) composite via a microwave-assisted strategy, achieving an EMI SE of 32.1 dB [21]. A comparative study of segregated and homogeneous CNT/polyethylene composites showed that the EMI SE of the former composite was 46% higher than the latter at the same CNT loading [22]. Segregated architecture is also considered an effective approach to construct continuous heat conduction networks. For example, Gao et al. reported a segregated structured BN/ultra-high molecular weight polyethylene (UHMWPE) composite which possesses a high TC of 5.7 W/m/K [23]. Wang et al. also constructed a segregated structure in UHMWPE with a hybrid conductive network, achieving a TC as high as 7.1 W/m/K [24]. Zhou et al. verified the efficient thermal transport along a three-dimensional conductive network in a segregated structure by comparing thermal transport ability with the homogenous composites, and an enhancement of TC from 6.2 to 17.8 W/m/K was achieved [25]. To sum up, it is an effective approach to develop the CPC with desirable thermal conductive or efficient EMI shielding properties by constructing a segregated network structure.

However, simultaneous amelioration of multifunctional performance is still a challenge in current segregated polymer composites. To our best knowledge, in pursuit of multifunctional properties, most segregated polymer composites are fabricated by incorporating a single nanomaterial with both high thermal and electrical conductivity, such as Ag nanoparticles [7,26], carbon nanotubes [5,27], graphene [28–30], and MXene [31,32]. Ascribed to the fact of phonon scattering arising from the high thermal interface resistance between the filler and the polymer matrix, the TC can be significantly improved only at large amounts of filler content, under which a percolative path is formed so that phonons can be transported through the percolated networks. Although a satisfactory EMI shielding ability can be assured, this also leads to ultrahigh electrical conductivity (EC) and a severe impedance mismatch. Thus, the assembly of hybrid fillers with different electrical and thermal properties is necessary to resolve the contradiction of thermal and electrical conductivity. Boron nitride and graphene with high thermal conductivities are effective fillers to upgrade the heat dissipation ability of composites. The incorporation of electrically

conductive graphene nanofillers can significantly improve the EMI shielding performance at low filler contents while inescapably increasing the electrical conductivity. Fortunately, boron nitride is an electrical insulator with an intrinsic wide bandgap of ≈ 5.5 eV. Therefore, the assembly of boron nitride and graphene with a rational structure design may be a promising way to escape the dilemma of electrical and thermal conductive incoordination.

Besides structural design, the engineering process is also crucial to the ultimate performance of polymer composites. Especially, the loaded pressure is an important processing parameter during conventional polymer processing and several studies have been adopted on pure polymers investigating the effects of pressure on their important properties such as crystallinity, rheology and mechanical properties [33–35]. Nevertheless, very little work has addressed the influence of processing pressure on the functionality of polymer composite materials.

In this work, multifunctional performance with the integration of outstanding EMI SE, low electrical conductivity, high TC, excellent thermal stability, enhanced tribological performance and satisfactory mechanical property is realized in BN/GNP/PPS composites. The BN/GNP dual-segregated network structure is first fabricated to resolve the contradiction of thermal and electrical conductivity. In addition, the effects of the mass ratio of BN to GNP and processing pressure on the microstructure and multi-functional performance have been investigated in detail. This work paves the way to fabricate high performance and multifunctional composites.

2. Materials and Methods

2.1. Materials

A commercial grade PPS with a weight-average molecular mass (M_w) and polydispersity (M_w/M_n) of 4.8×10^4 g/mol and ca. 2, respectively, was synthesized by the Sichuan Deyang Special New Material Co., Ltd (Deyang, China). BN, with the trade name BBN-30, was supplied by the Yaan Bestry Performance Materials Company (Shanghai, China). The average size of BN is approximately 26 μm . The GNP (KNG-182) with an average size of 35 μm was provided by the Xiamen Knano Graphene Technology Co., Ltd (Xiamen, China). All the chemicals used in this work are analytically pure and were used without further purification.

2.2. Preparation of BN/GNP/PPS Composites

Fabrication of the BN/GNP/PPS composites with a segregated structure is schematically depicted in Figure 1. BN/GNP/PPS composites with a filler content of 40 wt% were prepared by a two-step solid-state mechanical mixing process and then followed by a high-pressure hot compression shaping process. Initially, PPS particles with an average size of ~ 900 μm (see Figure 1a) were immersed in ethanol to wet the surface. The treated PPS particles were then mechanically mixed with GNP (Figure 1b) to prepare GNP-coated PPS complex particles. Subsequently, BN (Figure 1c) and GNP/PPS particles were mixed, achieving BN/GNP/PPS particles. The separated mixing processes were both conducted in a mechanical high-speed mixer for 4 min at a speed of 2500 rpm. After that, the BN/GNP/PPS particles were compression molded in a hot press for 480 min, under 0.1, 200, 600 and 1000 MPa, at a temperature of 350 $^\circ\text{C}$, to form cylindrical tablets (with a diameter of ~ 25 mm and a thickness of 3 mm, see Figure S1) for the following characterization. The BN/GNP filler loading was fixed at 40 wt%, while the BN and GNP weight ratios were 0:1, 1:3, 1:1, 3:1 and 1:0, respectively. For comparison, GNP and BN were uniformly mixed with PPS by melt blending using an internal mixer and compression molded under the same condition. For brevity, the ultimate composites with segregated structures were named $\text{BN}_x/\text{GNP}_y/\text{PPS}$ and uniformly mixed composites were named $\text{BN}_x/\text{GNP}_y/\text{PPS-UM}$, where x and y represent the weight contents of BN and GNP in the composites.

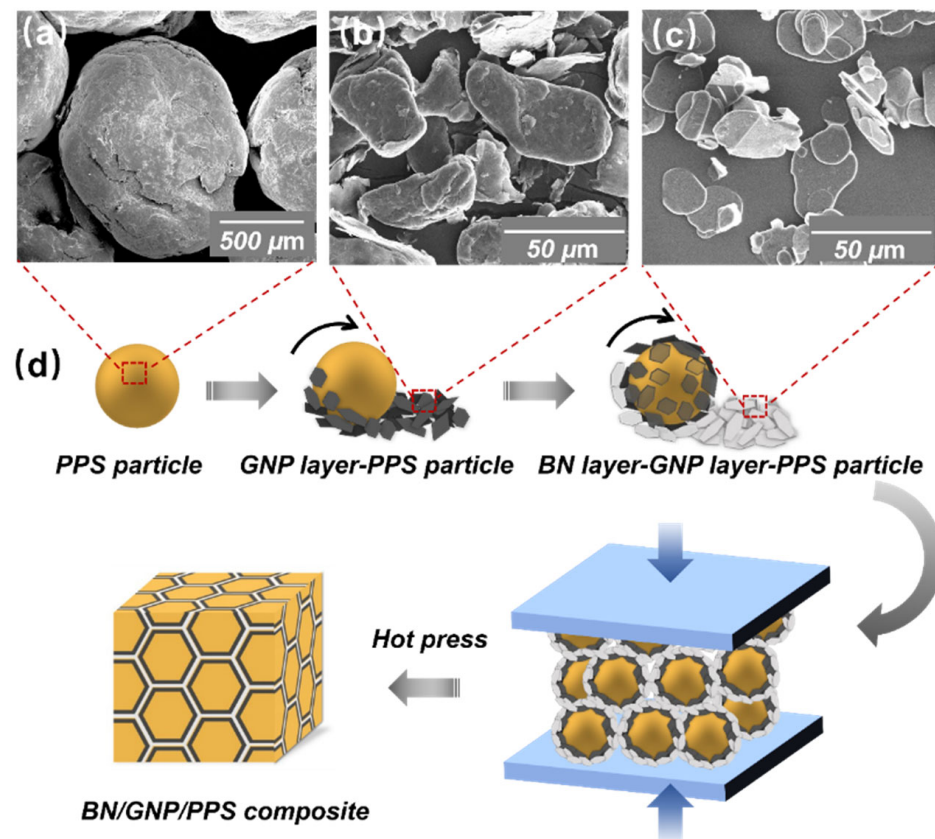


Figure 1. SEM images of (a) PPS particle, (b) GNP and (c) BN; (d) Schematic representation of fabrication process of BN/GNP/PPS composites with dual segregated structure.

2.3. Characterization

A field emission scanning electron microscopy (SEM, Inspect-F, FEI, Finland) was employed to reveal the freeze-fractured surfaces of PPS composites at an accelerating voltage of 5 kV. The fractured surfaces of the PPS composites were sprayed with gold nanoparticles before SEM observation. The composite sample was initially immersed in liquid nitrogen for 30 min and then quickly fractured. For optical microscopy (OM) measurement, the PPS composite specimens were cut into films of 20 μm thickness using a microtome and observed with an Olympus BX51 polarizing optical microscope (Olympus Co., Tokyo, Japan) with a Micro-Publisher 3.3 RTV CCD camera. The TC of the PPS composites was measured by a Hot Disk instrument (TPS2200, Gothenburg, Sweden) at 25 $^{\circ}\text{C}$. The sample size for TC measurement was 25.4 mm in diameter and 3 mm in thickness. The electrical resistance of the PPS composites was measured using a Keithley electrometer model 4200-SCS (Beaverton, OR, USA). The samples were cut into rectangular sheets, and the opposites were coated with silver paste to reduce the contact resistance. The electrical conductivity was calculated using the equation $\sigma = L/(S R)$, where σ and R represent the electrical conductivity and electrical resistance, and L and S are the length and cross-sectional area of the rectangular sheet. EMI shielding measurements were conducted in the frequency range of 8.2–12.4 GHz using an Agilent N5230 network analyzer (Palo Alto, CA, USA). The intermediate frequency bandwidth was set as 1 kHz during the measurement, and 201 points were collected for each specimen. Samples with 25.4 mm in diameter and 3 mm in thickness were placed in the specimen holder, which were connected through the Agilent 85132F coaxial line to separate VNA ports. The scattering parameters (S_{11} and S_{21}) of the PPS composites in the frequency range of 8.2–12.4 GHz (X-Band) were gained to calculate the EMI SE. A ball-on-disk friction and wear apparatus (SRV-IV tribo-tester, Optimol Instruments Prüftechnik GmbH, Munich, Germany) was used to measure the coefficient of friction (COF) of the BN/GNP/PPS composites. The ball, with a diameter

of 5.0 mm, was made of GCr15 steel. The BN/GNP/PPS composites with a diameter of 25.4 mm and a thickness of 3 mm were fixed on the stage. The experiments were conducted under dry friction conditions (temperature ~25 °C, relative humidity ~50%), stroke = 1 mm, normal load = 5 N, duration = 30 min and a sliding frequency 25 Hz. The COF was recorded with a computer. For each experimental condition, each test was carried out three times. The tests on each specimen were re-peated at least three times, after which the average COF was determined. An optical white light interferometer (NPFLEX) was employed to measure the volumes of the wear scar on the BN/GNP/PPS composite disk-like samples. The wear rate was calculated by dividing the wear volume per unit product of sliding distance and load.

3. Results and Discussion

3.1. Morphological and Structural Analysis

The optical microscopy images of all the PPS composites are shown in Figure S2. Well-designed dual-segregated structures are clearly observed. Considering the similarity of morphologies prepared under different pressures, we only chose composites under 600 MPa as examples for the following discussion. The optical micrographs of the BN/PPS, BN/GNP/PPS, GNP/PPS and BN/GNP/PPS-UM composites processed under 600 MPa are shown in Figure 2. The distribution of BN and GNP in the PPS composites can be easily identified due to the light transmittance difference; that is, the BN enriched region appears to be white, the GNP region appears to be dark, and the PPS appears to be gray. It is obvious that segregated structures exist in the BN/PPS, BN/GNP/PPS and GNP/PPS composites (Figure 2a–e) after compression molding, while BN and GNP are homogenously distributed in the BN/GNP/PPS-UM composite (Figure 2f). Since the filler content is as high as 40 wt%, the filler regions, distributed around the PPS interfaces, are dense and thick enough to form continuous networks. In the filler regions, the GNP and BN fillers are separately distributed rather than homogenously mixed, which is beneficial to a higher TC ascribed to the low phonon scattering at the interfaces of two identical fillers [1]. The rational assembly of BN and GNP in the segregated structure is realized by controlling the coating sequence in the mixing process. GNP is coated on the surface of PPS particles prior to BN, and thus GNP is distributed at the interface between PPS and BN domains. In other words, the GNP layer is coated by BN, and thus one may expect the low electrical conductivity and increased microwave adsorption ability of PPS composites. To observe the detailed microstructure of the interfaces, high-magnification SEM images were further taken, as shown in Figure 3. The interfaces of both PPS and GNP, as well as BN and GNP, are clearly visible in the PPS composites. The PPS particles were not broken up because of the weak flow during hot-pressing. In addition, high processing pressure is also responsible for the distinct interfaces. As depicted in Figure 3g–i, higher magnification images reveal the detailed information about the interfaces of GNP and PPS under different pressures. When compressed under low pressure (0.1 MPa), a relatively ambiguous interface is observed, demonstrating the diffusion of PPS chains into/across GNP particles at a lower pressure. With the increase of compression pressure, distinct stereological textures were observed. With the aid of high pressure, the filler component is squeezed into dense conductive channels, and bundles of GNP were observed to be clustered tightly, which effectively prevents the PPS from penetrating into the conductive filler area. In conclusion, ascribed to the weak flow as well as high processing pressure, the movement of PPS long molecular chains is confined, which would prevent the GNP from penetrating into PPS regions and ensure the selective distribution of GNP.

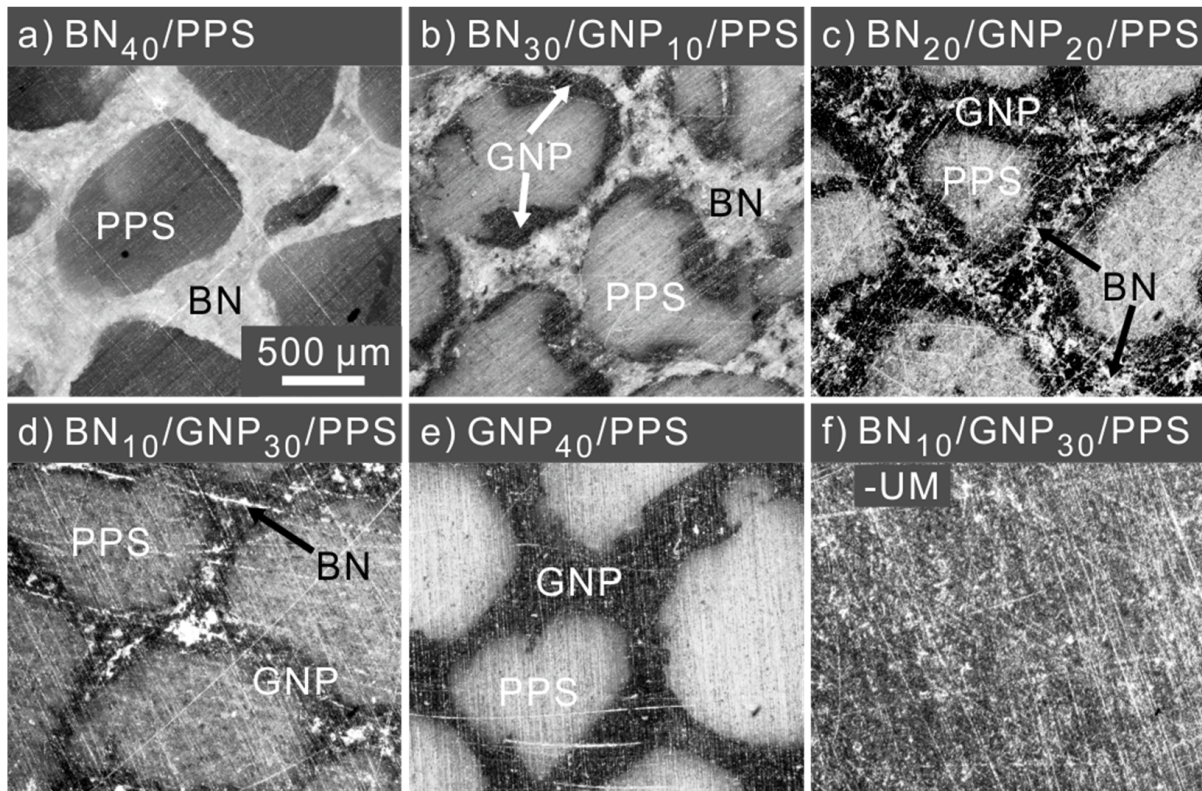


Figure 2. OM images of (a) BN₄₀/PPS, (b) BN₃₀/GNP₁₀/PPS, (c) BN₂₀/GNP₂₀/PPS, (d) BN₁₀/GNP₃₀/PPS, (e) GNP₄₀/PPS and (f) BN₁₀/GNP₃₀/PPS-UM composites processed under 600 MPa.

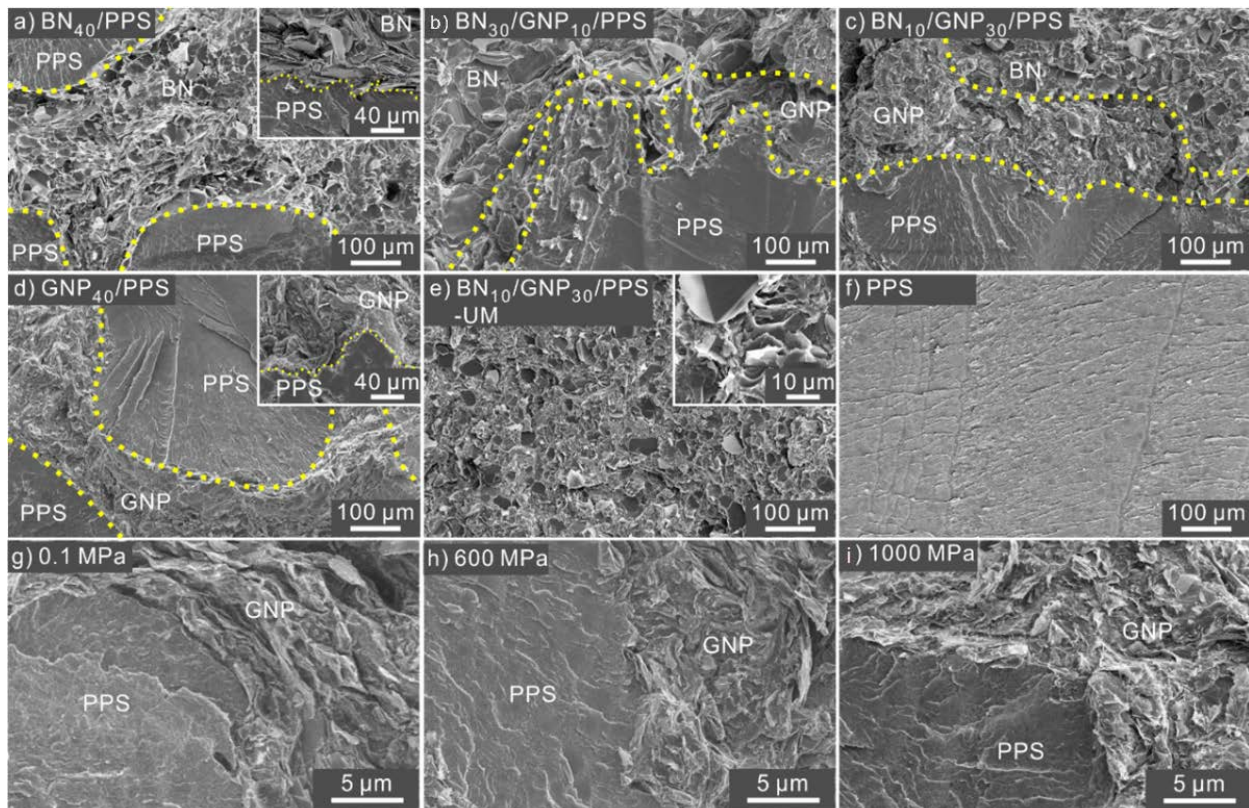


Figure 3. SEM images of PPS composites processed under 600 MPa (a–f) and GNP₄₀/PPS composite under different pressures (g–i).

3.2. Thermal Conductive Properties

Figure 4 presents the thermal conductivities of neat PPS, PPS composites with segregated structures, and the BN₁₀/GNP₃₀/PPS-UM composite, which are fabricated at different pressures. As shown in Figure 4a, neat PPS shows very low TCs, $\sim 0.3 \text{ Wm}^{-1}\text{K}^{-1}$, regardless of the processing pressures. The addition of GNP or BN fillers with inherently high thermal conductivities delivered excellent TC enhancement with respect to that of the pure PPS. For example, the TCs for BN₁₀/GNP₃₀/PPS-UM composites with randomly distributed fillers increased to approximately $4 \text{ Wm}^{-1}\text{K}^{-1}$, which is more than 10 times compared with neat PPS. More remarkably, the construction of segregated structures in PPS composites further improves the TC; it climbs up to $5\text{--}8 \text{ Wm}^{-1}\text{K}^{-1}$ depending on the processing pressure. Take 600 MPa as an example, the TC of BN₁₀/GNP₃₀/PPS is as high as $6.4 \text{ Wm}^{-1}\text{K}^{-1}$, which is significantly higher than the randomly distributed counterparts ($4.8 \text{ Wm}^{-1}\text{K}^{-1}$). The segregated distribution made BN and GNP form percolation so that phonons could be transported through the percolated networks rather than through the BN/PPS or GNP/PPS interfaces where a much higher thermal resistance is imposed. The results reveal that the design of the thermal conductive network in the polymer matrix is crucial for improving the thermal conductivity.

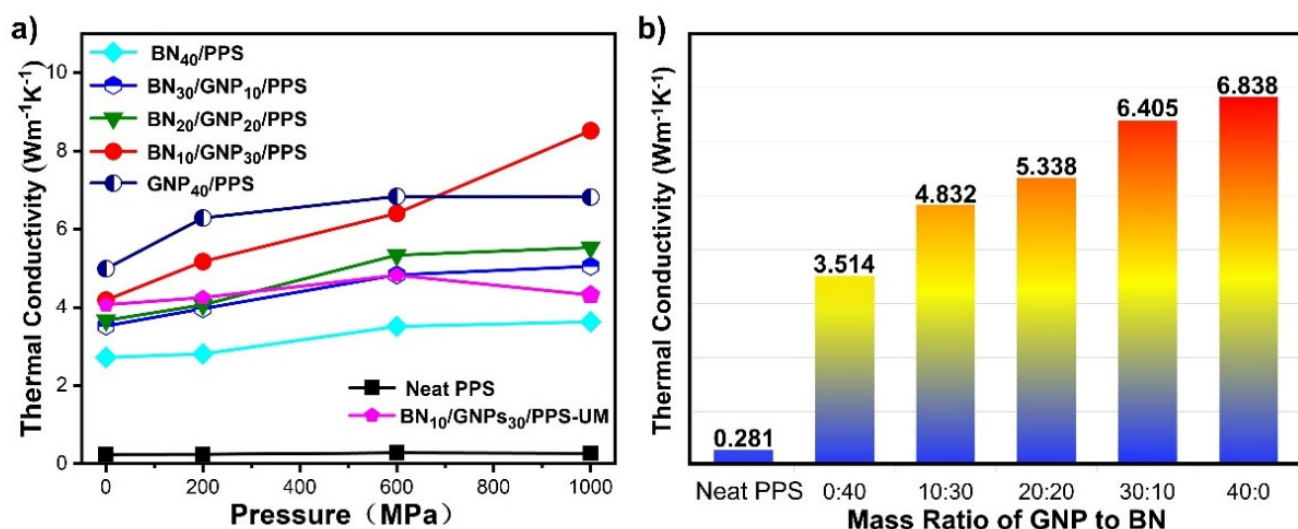


Figure 4. (a) Thermal conductivity of PPS composites with segregated structures (BN₄₀/PPS, BN₃₀/GNP₁₀/PPS, BN₂₀/GNP₂₀/PPS, BN₁₀/GNP₃₀/PPS, GNP₄₀/PPS), neat PPS and BN₁₀/GNP₃₀/PPS composites with uniformly-distributed fillers, which were fabricated at different pressures; (b) Thermal conductivity of neat PPS and PPS composites with different mass ratio of GNP to BN, which were processed under 600 MPa.

Another factor affecting TCs of polymer composites that has not been well recognized before is processing pressure. It clearly shows that TCs increase with the augmentation of processing pressure. Why do the TCs of PPS composites increase with the processing pressure? From the above SEM results, one may find that the high pressure has a positive effect on ameliorating the thermally conductive networks to be more compact and improve interfacial bonding between conductive fillers and the PPS matrix, which can effectively reduce the interfacial thermal resistance between filler–filler and filler–matrix. Moreover, the DSC heating curves in Figure S3 demonstrate an increase in the crystallinity of the PPS matrix when increasing the pressure, leading to a higher intrinsic TC of the PPS matrix [33]. In general, the increased packing density of fillers in the conductive network improved the thermal conductivity of the PPS matrix as well as reduced interfacial thermal resistance, ultimately ameliorating the TC of PPS composite. Intriguingly, pressure presents a more profound effect on PPS composites with segregated structures than uniformly mixed ones. Take BN₁₀/GNP₃₀/PPS and BN₁₀/GNP₃₀/PPS-UM

as examples, the TCs of BN₁₀/GNP₃₀/PPS and BN₁₀/GNP₃₀/PPS-UM are comparable under 0.1 MPa (4.2 Wm⁻¹K⁻¹ for BN₁₀/GNP₃₀/PPS, 4.1 Wm⁻¹K⁻¹ for BN₁₀/GNP₃₀/PPS-UM), with the pressure increasing to 1000 MPa, the TC of BN₁₀/GNP₃₀/PPS sharply increased to 8.5 Wm⁻¹K⁻¹, while only a small enhancement of 0.2 Wm⁻¹K⁻¹ is achieved in BN₁₀/GNP₃₀/PPS-UM. For the BN₁₀/GNP₃₀/PPS-UM composites, BN and GNP possess a random distribution with few connections to each other. The utilization of high pressure improves the contact possibility of neighboring fillers, reducing the phonon scattering to some extent and slightly improving the TC. While the high pressure is adopted to BN₁₀/GNP₃₀/PPS with a segregated structure, the fillers are effectively squeezed, which causes efficient phonon transport through the fillers. As the thermal resistance mainly originates from filler interfaces, higher interfacial thermal conductance between BN-BN or GNP-GNP can ultimately increase the thermal conductivities of PPS composites with segregated structures. Furthermore, by assembling GNP and BN fillers into the segregated structure, the thermal conductivities of PPS composites were further improved. Figure 4b clarifies how the assemble ratio affects the TCs. In comparison with BN, GNP has higher intrinsic TC. Keeping the total filler content fixed at 40 wt%, the TCs for composites under 600 MPa continuously climb up from 3.5 Wm⁻¹K⁻¹ to 6.8 Wm⁻¹K⁻¹ with the increased GNP content. It is worth noting that the synergistic enhancement effect of BN and GNP is stimulated under high pressure. For example, the TC for BN₁₀/GNP₃₀/PPS is comparable with that of GNP₄₀/PPS under 600 MPa, and it far outstrips the value of GNP₄₀/PPS when the pressure increases to 1000 MPa, reaching a conductivity of 8.5 Wm⁻¹K⁻¹, which is 25% and 136% higher than GNP₄₀/PPS and BN₄₀/PPS. It is speculated that the intercalation structure is formed under high pressure and the interfacial thermal resistance between the neighboring GNP is effectively reduced by the insertion of lamellar BN. In general, the combination of segregated structures, the rational assemble of GNP with BN and high processing pressure have a synergetic effect on attaining a high TC for PPS composite. It is worth mentioning that although the TC has been elevated to a large extent compared with pure PPS, it is still far lower than the intrinsic TC of both BN and GNP, which is ascribed to the limitation of filler content and thermal interface resistance. With increasing filler content, the TC of PPS composites could continuously be further improved, but a high filler loading could compromise mechanical flexibility and processibility. Therefore, the filler content in PPS composites should be maintained to achieve a balance between thermal conductivity and the desired multifunctional properties. On the other hand, interfacial thermal resistance is an important part of influencing the TC of PPS composites, which includes those between BN and BN, GNP and GNP, BN and GNP, BN and PPS matrix and GNP and PPS matrix. Efforts can be made to reduce the phonon scattering at the interfaces, such as the construction of percolative paths and the rational distribution of BN and GNP. Nevertheless, heat loss is inevitable as long as there are interfaces.

To visualize this heat dissipation difference, infrared imaging was used to record the temperature response during heating, as shown in Figure 5. We can clearly see that the surface temperatures of PPS composites with segregated structured conductive networks rise much faster than the uniformly mixed PPS composite and neat PPS, following the sequence: GNP₄₀/PPS > BN₁₀/GNP₃₀/PPS > BN₄₀/PPS > BN₁₀/GNP₃₀/PPS-UM > PPS. This transient temperature response agrees well with the thermal conductivity (Figure 4). The surface temperatures of BN₁₀/GNP₃₀/PPS, BN₁₀/GNP₃₀/PPS-UM and PPS were scanned from the bottom along the white dotted line (see Figure 5a), as plotted in Figure 5b. The BN₁₀/GNP₃₀/PPS presents a more homogenous temperature distribution compared with the BN₁₀/GNP₃₀/PPS-UM and PPS, that is, a relatively lower temperature near the heating source while there is a higher temperature far from the heating source, indicating better thermal diffusion and dissipation capacity. Overall, the conclusion can be brought to light that BN/GNP/PPS composites with dual-segregated structures processed under high pressure allow for efficient heat transferring and dissipating, showing a bright prospect as the thermal conductive media for next-generation microelectronic devices.

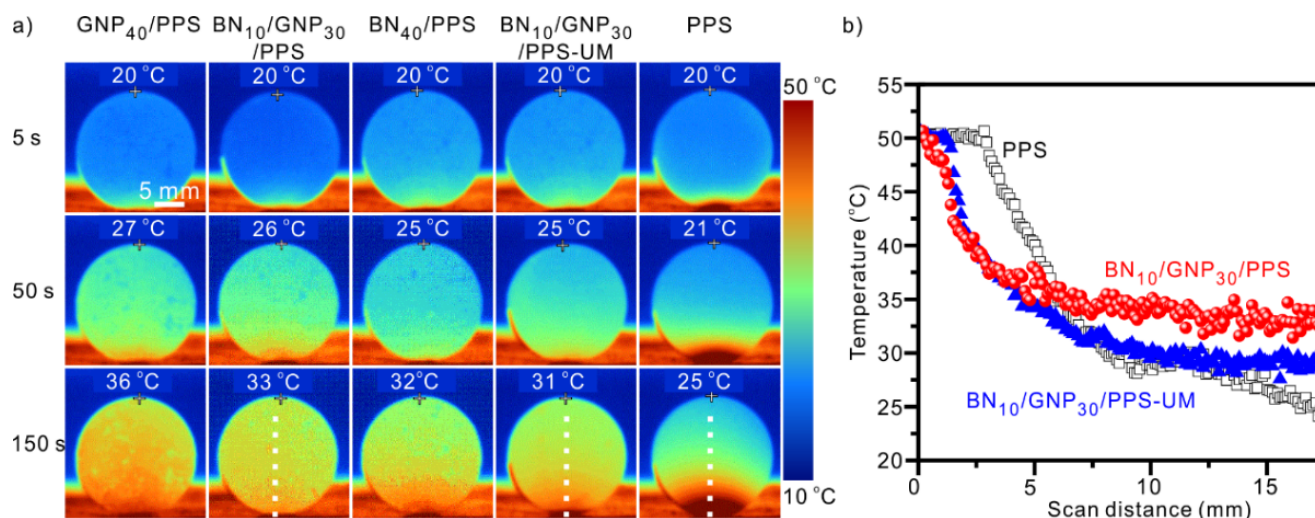


Figure 5. (a) Infrared thermal images of PPS and PPS composites processed under 600 MPa during the heating process and (b) surface temperature variation as a function of heating distance.

3.3. Electrical Conductivity and EMI Shielding Performance of PPS Composites

The electrical conductivity of PPS composites as a function of pressure is shown in Figure 6. The electrical conductivities of neat PPS and BN₄₀/PPS composites are kept constantly at $\sim 10^{-13}$ S/m, ascribed to the insulation property of PPS and BN. With the introduction of GNP content, the electrical conductivity increased monotonically. In addition, the segregated structured composites present higher electrical conductivity and increase in the wake of ascending pressure, while the uniformly mixed composites and neat PPS are stubborn to pressure. For example, the electrical conductivity for BN₃₀/GNP₁₀/PPS display a significant increase of approximately 2 orders of magnitude (from 6.7×10^{-4} S/m to 0.019 S/m) when the pressure rises from 0.1 MPa to 1000 MPa. Given the same filler content, an increment of 51% from 0.055 S/m to 0.083 S/m is achieved in the BN₁₀/GNP₃₀/PPS composites, while there is no obvious change for BN₁₀/GNP₃₀/PPS-UM with the increase in processing pressure. Despite the compression of the conductive network at high pressure, the electrical conductivity is still far lower than traditional segregated structured EMI-shielding materials (Table S1), which is ascribed to the insulating BN layers that break the GNP conducting network.

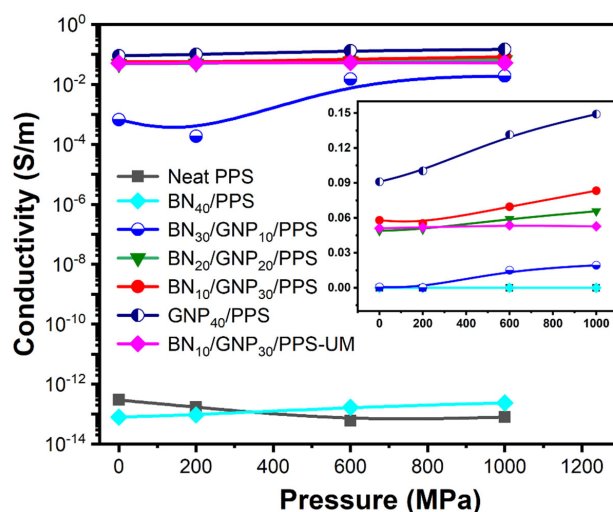


Figure 6. Electrical conductivities of PPS composites with segregated structures (BN₄₀/PPS, BN₃₀/GNP₁₀/PPS, BN₂₀/GNP₂₀/PPS, BN₁₀/GNP₃₀/PPS, GNP₄₀/PPS), neat PPS and BN₁₀/GNP₃₀/PPS-UM composites and inset is the conductivities shown on a linear scale.

It is well acknowledged that electrical conductivity is one of the critical parameters affecting electromagnetic interference shielding. Surprisingly, despite the relatively low electrical conductivity, satisfying electromagnetic interference shielding effectiveness (EMI SE) is achieved in PPS composites, as shown in Figure 7. With 10 wt% GNP loading, the EMI SE surpasses the standard value for commercial applications (20 dB), and the increasing GNP content directly causes higher EMI SE. The maximum EMI SE at 30 wt% GNP is 70 dB, which is quite a high level compared with previously reported works (as summarized in Table S1). It is worth mentioning that all of the efforts made in this work, including the construction of segregated conductive network, the adoption of high pressure and the rational assembly of BN and GNP, contribute to the excellent EMI shielding performance. Sharing the same component composition, the BN₁₀/GNP₃₀/PPS composite featuring a segregated structure presents a superb SE of 70 dB, while a lower value of 54 dB is achieved for the BN₁₀/GNP₃₀/PPS-UM composite in which fillers are uniformly distributed, indicating the ascendancy of the segregated structure on EMI shielding. The localized distribution of GNP in a segregated structure can greatly enhance the utilization ratio, leading to increased electrical conductivity of the composite. More importantly, the densely packed GNP networks at the interfaces can effectively interact with incident radiation, leading to the very high EMI SE. Furthermore, Table S1 gives a comparison of the EMI SE of composites with segregated structures, in which our data outperforms most previously published values. The superiority of BN/GNP/PPS composites constructed in our work may originate from the adoption of high pressure during the hot-pressing process. First of all, high pressure can directly contribute to more continuous and denser conductive networks, which is favorable for the sufficient interaction of interconnected GNPs with incoming electromagnetic waves, accordingly, leading to higher EMI SE. As verified in Figure 7b, with the increase of processing pressure, the SE for BN₁₀/GNP₃₀/PPS composite climbs sharply from 47.7 dB for 0.1 MPa to 67.8 dB for 1000 MPa. In addition, it is well known that the EMI SE of a shielding material is considerably pertinent to the filler content. Nevertheless, ascribed to the solidity and nondeformability of functional fillers, too much of them is adverse to the adhesion of polymer particles in a segregated structure. Applying high pressure can effectively help escape from the dilemma by strengthening the GNP-BN as well as GNP-PPS binding forces, and the filler content in this work can be as high as 40 wt%. Consequently, more conductive fillers participate in blocking incidental electromagnetic waves and directly result in higher EMI SE. It is noticeable that the EMI SE of BN₁₀/GNP₃₀/PPS is even higher than that of GNP₄₀/PPS, thus we comment that synergistic enhancement in the EMI SE was achieved by the BN and GNP dual segregated structure.

In order to reveal the shielding mechanism of PPS composites, total SE (SE_T), microwave reflection SE (SE_R) and microwave absorption (SE_A) of PPS composites are illustrated in Figure 7c,d. The SE_T , SE_A and SE_R of BN₁₀/GNP₃₀/PPS under 600 MPa are 67.4 dB, 60.5 dB and 6.9 dB, respectively. For comparison, the values of the BN₁₀/GNP₃₀/PPS-UM and GNP₄₀/PPS are also presented. GNP₄₀/PPS presents the highest SE_R , which is consistent with conductivities and attributed to the improved impedance mismatch between shielding surface and air. However, the SE_A of BN₁₀/GNP₃₀/PPS is superior to both BN₁₀/GNP₃₀/PPS-UM and GNP₄₀/PPS. This implies that the superior EMI shielding performance of BN₁₀/GNP₃₀/PPS can be attributed to the synergistic effect of the segregated structure and the hybrid of conductive fillers. By constructing a segregated structure, well developed conducting networks are formed, which is favorable for the ohmic loss and the special architecture provides many interfaces to reflect, scatter and absorb incident microwaves in the segregated unit cells. Moreover, as speculated in the former part, intercalation structure is formed under high pressure, thus the insertion of BN nanosheets into the GNP conductive network could generate more interfaces and act as defects. Owing to the large contrast in electrical conductivity between BN and GNP, free space charges can spontaneously accumulate at the interfaces under the electromagnetic field, which will induce the interfacial polarization effect and dipole polarization effect. It is worth noting that although SE_A is far higher than SE_R , this does not mean that the shielding mechanism

is adsorption dominated, since SE_A and SE_R only represent the ability of absorption loss and reflection loss [36]. As the processing pressure increases, the reflection effectiveness is almost unchanged, while the average SE_T was significantly promoted from 47.7 dB for 0.1 MPa to 67.8 dB for 1000 MPa. Thus, the enhanced EMI shielding performance is mainly attributed to the enhanced adsorption loss. Such enhancement indicates that the adoption of high pressure could significantly promote the SE_A by conductive loss, which is closely related to the interconnected GNP conductive networks. Specifically, the conducting network becomes more perfect after high pressure loading and could dissipate more electromagnetic energy by conductive loss. Meanwhile, the distinct interfaces of GNP-BN in the intercalation structure formed under high pressure can effectively initiate the accumulation of charge at the heterogeneous interfaces, resulting in enhanced interfacial polarization loss. In general, excellent EMI shielding performance with low electrical conductivity and decreased SE_R is realized by rationally assembling GNP with BN in a segregated structured composite under high pressure.

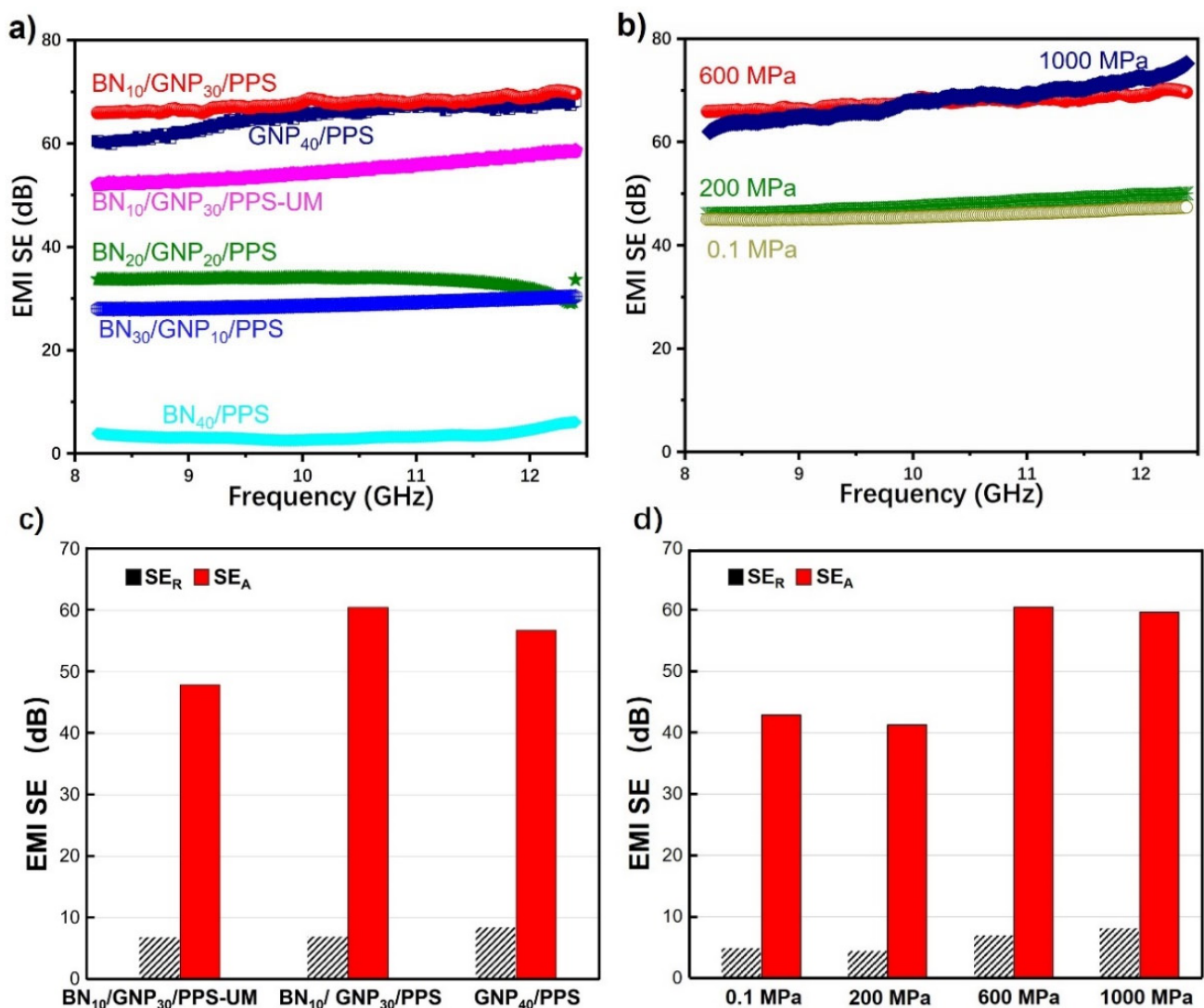


Figure 7. EMI shielding effectiveness of (a) PPS composites with segregated structures (BN₄₀/PPS, BN₃₀/GNP₁₀/PPS, BN₂₀/GNP₂₀/PPS, BN₁₀/GNP₃₀/PPS, GNP₄₀/PPS), neat PPS and BN₁₀/GNP₃₀/PPS-UM composites with uniformly-distributed fillers fabricated under 600 MPa, (b) BN₃₀/GNP₁₀/PPS composites fabricated under different pressures, (c) SE_T , SE_A and SE_R of BN₁₀/GNP₃₀/PPS-UM, BN₁₀/GNP₃₀/PPS and GNP₄₀/PPS composites fabricated under 600 MPa, and (d) SE_T , SE_A and SE_R of BN₁₀/GNP₃₀/PPS composites as a function of pressure.

It has become a critical design factor for miniaturized electronic components to incorporate EMI shielding and heat dissipation into the same part. Therefore, materials simultaneously endowing high EMI SE and TC are urgently needed. Figure 8a presents a comparison of EMI SE and TC obtained in this work and previously reported in the literature (detailed information can be seen in Table S2 in Supporting Information). Encouragingly, our fabricated BN/GNP/PPS composites simultaneously achieved superior EMI SE and TC.

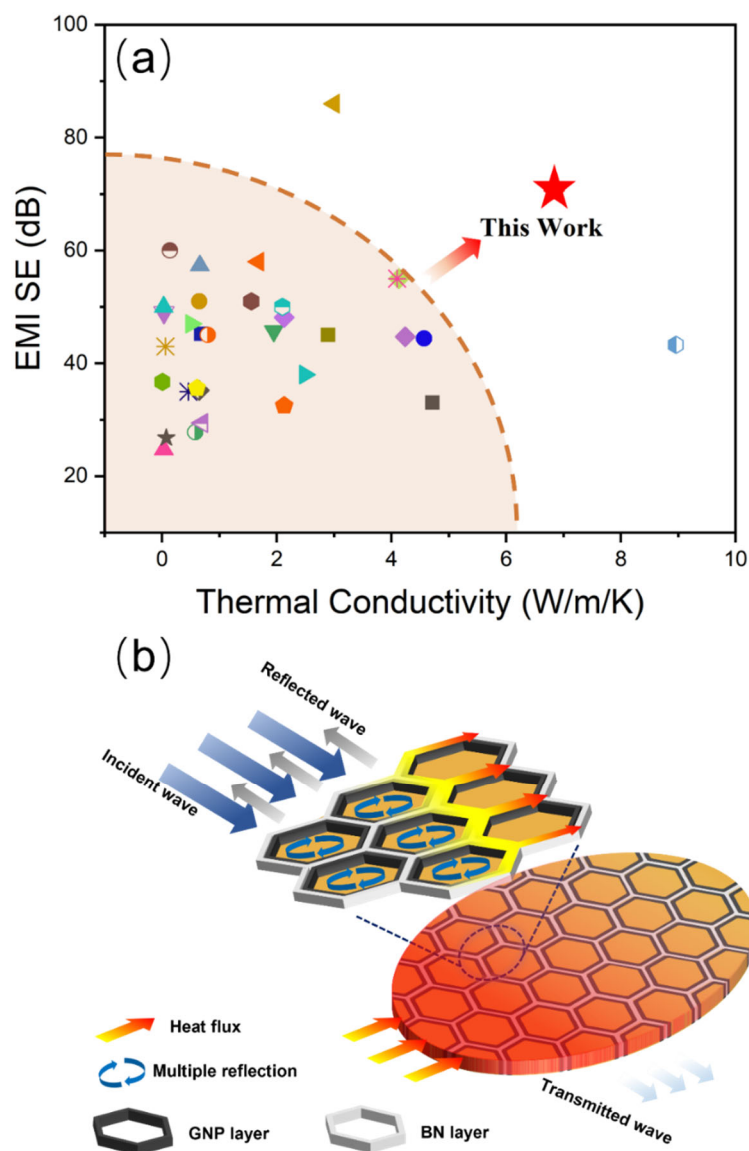


Figure 8. (a) Comparison of EMI SE and thermal conductivity of BN/GNP/PPS composites with other reported composites (detailed information in Table S2 in Supporting Information), (b) Schematic illustration of the EMI shielding mechanism for BN/GNP/PPS composites with segregated structure.

Schematic illustrations of thermal conduction and the EMI shielding mechanism are shown in Figure 8b. The synchronous realization of satisfying thermal conductive and EMI shielding performance is attributed to the well-defined segregated structure. Since both GNP and BN have excellent thermal conductivity, a perfect 3D thermal conductive path is formed by GNP and BN dual-segregated structures, which provides an expressway for phonon conduction. In addition, GNP and BN are separately distributed in the interface of PPS, which is favorable for minimizing the interfacial thermal resistance between GNP and BN fillers. Moreover, the application of high pressure can effectively improve the interfacial

bonding and release the interstice inside composites, greatly reducing the phone scattering at interfaces or void defects.

The dual-segregated structures also play a crucial role in EMI shielding. When microwaves are incident on the surface of PPS composites, some of them are reflected and residual enters the material. Then, incident microwaves are trapped inside the segregated unit cells and dissipated in the form of heat by multiple reflection and scattering. At the same time, the heat transformed from incident microwaves could be dissipated quickly through conductive networks. Therefore, the BN/GNP/PPS composites with superior EMI shielding performance and excellent thermal management performance are expected to find a wide range of potential applications in the fields of the communication industry, artificial intelligence and wearable electronics.

3.4. Tribological, Mechanical and Thermal Properties

Aside from the outstanding thermal conductivity and the excellent EMI shielding properties, we also investigate the wear-resisting performance, mechanical properties and thermal stability of PPS composites. Good wear resistance is important for a material applied in a harsh environment. Hence, the tribological properties of these PPS composites were studied by using a ball-on-disk friction and wear apparatus. Two main performance indicators of COF and wear rate are shown in Figure 9. The homogenous mixed PPS composites show lower COF than neat PPS because the layer structures of both GNP and BN can work together with the PPS matrix and form a stable lubricating layer on the wear surfaces, which has been verified by the OM observations of the wear surfaces (Figure S4). Intriguingly, the COF of PPS composites with segregated structures further decreases by 50% compared with the uniformly-mixed PPS composites, which is as low as 0.03 for the BN₂₀/GNP₂₀/PPS composite processed under 0.1 MPa, indicating that the segregation between layer-structured filler and the PPS matrix is able to attain good lubrication effect. The improved wear resistance performance of the segregated PPS composite mainly comes from the good thermal conductivity and the densely packed BN and GNP layers. During the fraction process, an instantaneous high temperature is generated and softens the surface of PPS composites. Therefore, it is easy for the steel ball to make the friction surface rough, leading to a large friction coefficient. In the case of BN/GNP/PPS composites, the GNP and BN dual-segregated structure with excellent thermal conductivity can transform the heat immediately, which is effective to elevate the friction performance. In addition, a small amount of BN and GNP will migrate out from the densely-packed networks and form a transfer film between the steel ball and the wear surface, which can provide reliable protection for the PPS matrix, thus decreasing the surface roughness and friction coefficient of the friction surface. However, an excessive amount of BN and GNP may exfoliate from the friction surface in the homogenous mixed PPS composites, which inevitably causes an increased friction coefficient. Both the PPS composites and neat PPS processed under 0.1 MPa and 200 MPa show a lower COF than those processed under 600 MPa and 1000 MPa. The reason for the increased COF of PPS samples processed under 600 MPa and 1000 MPa is likely to be caused by the increased crystallinity of PPS. As shown in Figure S3, the crystallinity of both neat PPS and PPS composites increases from 50% for 0.1 MPa and 200 MPa to 80% for 600 MPa and 1000 MPa, resulting in the less flexible PPS matrix to form a lubricating layer. However, the negative effect of high pressure on BN₁₀/GNP₃₀/PPS is negligible, which presents a COF as low as 0.05 under 600 MPa and 1000 MPa. Figure 9b shows the wear rate of both PPS composites and neat PPS. Even though the COF varied with the loading of fillers and the segregated structures, it is clear that the wear rates of these PPS samples are, in fact, at the same level ($\sim 10^{-5} \text{ mm}^3 \text{N}^{-1} \text{m}^{-1}$), which is in the range of the reported wear rate of PPS. This may be due to the similar wear mechanism, that is, the adhesive–abrasive mechanism of all the PPS composite samples, as the wear surfaces show adhesion and micro-cutting (Figure S4).

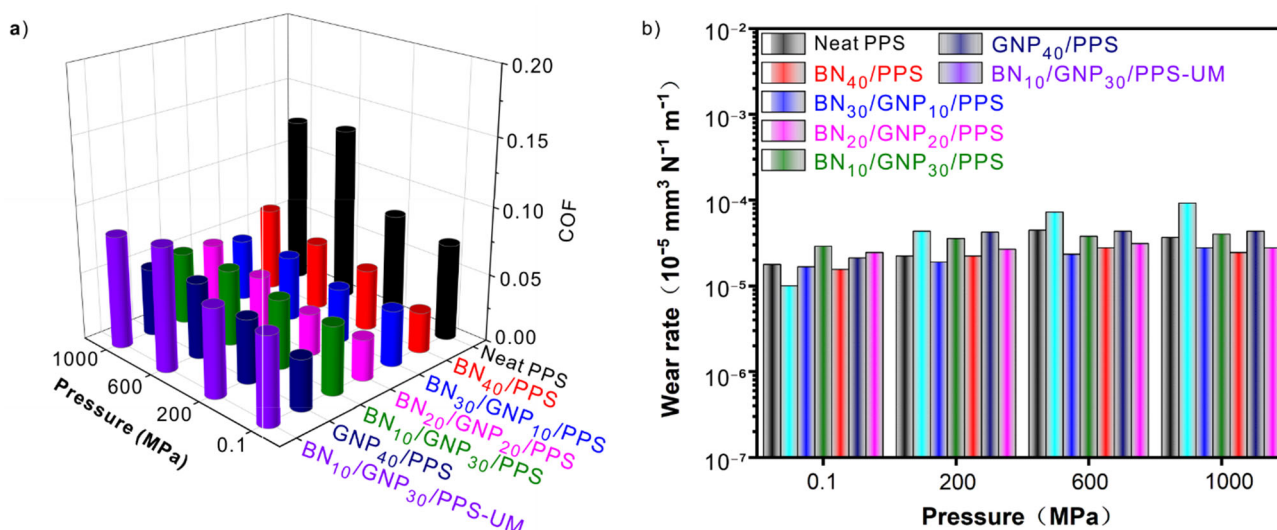


Figure 9. The tribological performance of PPS composites with segregated structures (BN₄₀/PPS, BN₃₀/GNP₁₀/PPS, BN₂₀/GNP₂₀/PPS, BN₁₀/GNP₃₀/PPS, GNP₄₀/PPS), neat PPS and BN₁₀/GNP₃₀/PPS-UM composites with uniformly-distributed fillers, which were fabricated at different pressures. (a) COF, (b) Wear rate.

In addition to wear resistance, mechanical properties are also essential for practical application. It is reported that conventional segregated structured composites fabricated by solid mixing and thermoforming technology always present seriously deteriorated mechanical properties due to the weak interaction between the polymer matrix and conductive fillers. In the current work, with the filler content as high as 40 wt%, only a slight decrease in the compressive strength for segregated PPS composites is observed, which can reach 146 MPa (Table S3, Supplementary Materials), outperforming most segregated polymer composites.

The thermal stability of PPS composites was also investigated. The TGA curves of neat PPS and composites are shown in Figure S5. Both neat PPS and composites maintain their stability up to ~ 480 °C and are pyrolyzed in the temperature range of 500–600 °C. The addition of conductive fillers can further increase the thermal degradation temperature ascribed to the thermal protection effect of GNP and BN. No significant influence of the processing pressures on the thermal stability was observed. These results indicate that the PPS composites inherit the excellent thermal stability of PPS resin.

Overall, the composites not only present simultaneously excellent thermal conductive and EMI shielding performance but also multi-functional performance by integrating good wear resistance performance, mechanical properties and thermal stability.

4. Conclusions

In summary, multifunctional PPS composites have been fabricated under the strategies of dual segregated structure construction and high-pressure molding. Efficient thermal transport is realized in segregated PPS composites, reaching a thermal conductivity as high as 8.5 W/m/K. Meanwhile, the electrical conductivity is significantly decreased, which is much lower than previously reported segregated polymer composites with a single filler. The segregated dual network structure and high pressure are also favorable for EMI performance by creating numerous interfaces for microwaves, reflecting scattering and absorption, and a remarkable EMI SE of 70 dB is achieved. Moreover, the composites also have an excellent anti-fracture ability with a COF of 0.03, mechanical properties with a compressive strength as high as 146 MPa, and thermal stability up to 480 °C. The excellent comprehensive properties make it promising for PPS composites applied in new generation portable and miniaturized electronic devices.

Supplementary Materials: The following supporting information can be downloaded at: <https://www.mdpi.com/article/10.3390/nano12193543/s1>, Figure S1: Digital images of cylindrical tablets of PPS composites hot pressed under different pressures; Figure S2: OM images of PPS composites processed under different pressures; Table S1: Integrated comparison of electrical conductivity and EMI SE among BN/GNP/PPS composites and other previous reported polymer composites with segregated structure; Table S2: Integrated comparison of thermal conductivity and EMI SE among BN/GNP/PPS composites and other previous reported polymer composites; Figure S3: DSC heating curves of BN₁₀/GNP₃₀/PPS with segregated structures and neat PPS processed under different pressures; Figure S4: OM observations of worn surfaces of PPS composites and neat PPS after the test; Figure S5: TGA curves of Neat PPS and GNP/BN/PPS composites at 200 MPa, TGA curves of Neat PPS and GNP₃₀/BN₁₀/PPS composites under different molding pressures; Table S3: The compressive strength of neat PPS and PPS composites processed under different pressures. References [37–85] are cited in the supplementary materials.

Author Contributions: Conceptualization, Y.C.; methodology, L.Z., Y.C. and K.Z.; validation, S.Y.; formal analysis, S.Y.; investigation, L.Z. and S.Y.; resources, K.Z.; data curation, L.Z. and S.Y.; writing—original draft preparation, L.Z.; writing—review and editing, S.Y. and Y.C.; visualization, L.P.; supervision, Y.C. All authors have read and agreed to the published version of the manuscript.

Funding: This research was funded by the National Natural Science Foundation of China (21978240, 21676217, 52003215, and 52103127), the Fundamental Research Funds for the Central Universities, the Open Testing Foundation of the Analytical & Testing Center of Northwestern Polytechnical University (No. 2020T020), the Key Research and Development Program of Shaanxi (No. 2021GY-239), the Natural Science Basic Research Program of Shaanxi (No. 2021JQ-564), and the Opening Project of State Key Laboratory of Polymer Materials Engineering (Sichuan University) (No. sklpm2022-4-10).

Institutional Review Board Statement: Not applicable.

Informed Consent Statement: Not applicable.

Data Availability Statement: The data presented in this study are available on request from the corresponding author.

Conflicts of Interest: The authors declare no conflict of interest.

References

1. Guo, F.M.; Shen, X.; Zhou, J.M.; Liu, D.; Zheng, Q.B.; Yang, J.L.; Jia, B.H.; Lau, A.K.T.; Kim, J.K. Highly thermally conductive dielectric nanocomposites with synergistic alignments of graphene and boron nitride nanosheets. *Adv. Funct. Mater.* **2020**, *30*, 1910826. [[CrossRef](#)]
2. Li, X.; Li, C.H.; Zhang, X.M.; Jiang, Y.P.; Xia, L.C.; Wang, J.F.; Song, X.D.; Wu, H.; Guo, S.Y. Simultaneously enhanced thermal conductivity and mechanical properties of PP/BN composites via constructing reinforced segregated structure with a trace amount of BN wrapped PP fiber. *Chem. Eng. J.* **2020**, *390*, 124563. [[CrossRef](#)]
3. Nan, B.F.; Wu, K.; Qu, Z.C.; Xiao, L.Q.; Xu, C.G.; Shi, J.; Lu, M.G. A multifunctional thermal management paper based on functionalized graphene oxide nanosheets decorated with nanodiamond. *Carbon* **2020**, *161*, 132–145. [[CrossRef](#)]
4. Yuan, Y.; Sun, X.X.; Yang, M.L.; Xu, F.; Lin, Z.S.; Zhao, X.; Ding, Y.J.; Li, J.J.; Yin, W.L.; Peng, Q.Y.; et al. Stiff, thermally stable and highly anisotropic wood-derived carbon composite monoliths for electromagnetic interference shielding. *ACS Appl. Mater. Int.* **2017**, *9*, 21371–21381. [[CrossRef](#)]
5. Wang, Z.G.; Yang, Y.L.; Zheng, Z.L.; Lan, R.T.; Dai, K.; Xu, L.; Huang, H.D.; Tang, J.H.; Xu, J.Z.; Li, Z.M. Achieving excellent thermally conductive and electromagnetic shielding performance by nondestructive functionalization and oriented arrangement of carbon nanotubes in composite films. *Compos. Sci. Technol.* **2020**, *194*, 108190. [[CrossRef](#)]
6. Li, J.; Wang, Y.; Yue, T.N.; Gao, Y.N.; Shi, Y.D.; Shen, J.B.; Wu, H.; Wang, M. Robust electromagnetic interference shielding, joule heating, thermal conductivity, and anti-dripping performances of polyoxymethylene with uniform distribution and high content of carbon-based nanofillers. *Compos. Sci. Technol.* **2021**, *206*, 108681. [[CrossRef](#)]
7. Ren, W.; Yang, Y.Q.; Yang, J.; Duan, H.J.; Zhao, G.Z.; Liu, Y.Q. Multifunctional and corrosion resistant poly(phenylene sulfide)/Ag composites for electromagnetic interference shielding. *Chem. Eng. J.* **2021**, *415*, 129052. [[CrossRef](#)]
8. Wang, X.X.; Cao, W.Q.; Cao, M.S.; Yuan, J. Assembling nano-microarchitecture for electromagnetic absorbers and smart devices. *Adv. Mater.* **2020**, *32*, 2002112. [[CrossRef](#)]
9. Gorrasi, G.; Bugatti, V.; Milone, C.; Mastrorlando, E.; Piperopoulos, E.; Iemmo, L.; Di Bartolomeo, A. Effect of temperature and morphology on the electrical properties of PET/conductive nanofillers composites. *Compos. Part B-Eng.* **2018**, *135*, 149–154. [[CrossRef](#)]

10. Yao, T.; Zhou, W.; Peng, W.; Zhou, J.; Li, T.; Wu, H.; Zheng, J.; Lin, N.; Liu, D.; Hou, C. Insights into concomitant enhancements of dielectric properties and thermal conductivity of PVDF composites filled with Core@Double-Shell structured Zn@ZnO@PS particles. *J. Appl. Polym. Sci.* **2022**, e53069. [[CrossRef](#)]
11. Liu, H.; Du, H.; Zhao, W.; Qiang, X.; Zheng, B.; Li, Y.; Cao, B. Fast potassium migration in mesoporous carbon with ultrathin framework boosting superior rate performance for high-power potassium storage. *Energy Storage Mater.* **2021**, *40*, 490–498. [[CrossRef](#)]
12. Zhou, W.Y.; Li, T.; Yuan, M.X.; Li, B.; Zhong, S.L.; Li, Z.; Liu, X.R.; Zhou, J.J.; Wang, Y.; Cai, H.W.; et al. Decoupling of inter-particle polarization and intra-particle polarization in core-shell structured nanocomposites towards improved dielectric performance. *Energy Storage Mater.* **2021**, *42*, 1–11. [[CrossRef](#)]
13. Zhang, Y.L.; Ruan, K.P.; Gu, J.W. Flexible sandwich-structured electromagnetic interference shielding nanocomposite films with excellent thermal conductivities. *Small* **2021**, *17*, 2101951. [[CrossRef](#)]
14. Wang, G.; Liao, X.; Yang, J.M.; Tang, W.Y.; Zhang, Y.; Jiang, Q.Y.; Li, G.X. Frequency-selective and tunable electromagnetic shielding effectiveness via the sandwich structure of silicone rubber/graphene composite. *Compos. Sci. Technol.* **2019**, *184*, 107847. [[CrossRef](#)]
15. Zhang, L.Q.; Yang, B.; Teng, J.; Lei, J.; Yan, D.X.; Zhong, G.J.; Li, Z.M. Tunable electromagnetic interference shielding effectiveness via multilayer assembly of regenerated cellulose as a supporting substrate and carbon nanotubes/polymer as a functional layer. *J. Mater. Chem. C* **2017**, *5*, 3130–3138. [[CrossRef](#)]
16. Zhang, F.D.; Ren, P.G.; Guo, Z.Z.; Wang, J.; Chen, Z.Y.; Zong, Z.; Hu, J.; Jin, Y.L.; Ren, F. Asymmetric multilayered mxene-agnws/cellulose nanofiber composite films with antibacterial properties for high-efficiency electromagnetic interference shielding. *J. Mater. Sci. Technol.* **2022**, *129*, 181–189. [[CrossRef](#)]
17. Zhang, L.Q.; Yang, S.G.; Li, L.; Yang, B.; Huang, H.D.; Yan, D.X.; Zhong, G.J.; Xu, L.; Li, Z.M. Ultralight cellulose porous composites with manipulated porous structure and carbon nanotube distribution for promising electromagnetic interference shielding. *ACS Appl. Mater. Int.* **2018**, *10*, 40156–40167. [[CrossRef](#)]
18. Zeng, Z.H.; Jin, H.; Chen, M.J.; Li, W.W.; Zhou, L.C.; Xue, X.; Zhang, Z. Microstructure design of lightweight, flexible, and high electromagnetic shielding porous multiwalled carbon nanotube/polymer composites. *Small* **2017**, *13*, 1701388. [[CrossRef](#)]
19. Jia, L.; Ding, X.; Sun, J.; Zhang, X.; Tian, X.Y. A controllable gradient structure of hydrophobic composite fabric constructed by silver nanowires and polyvinylidene fluoride microspheres for electromagnetic interference shielding with low reflection. *Compos. Part A Appl. Sci. Manuf.* **2022**, *156*, 106884. [[CrossRef](#)]
20. Yan, D.X.; Pang, H.; Li, B.; Vajtai, R.; Xu, L.; Ren, P.G.; Wang, J.H.; Li, Z.M. Structured reduced graphene oxide/polymer composites for ultra-efficient electromagnetic interference shielding. *Adv. Funct. Mater.* **2015**, *25*, 559–566. [[CrossRef](#)]
21. Hu, Y.L.; Feng, D.; Xie, Y.H.; Xie, D.L. Microwave-assisted confining flame-retardant polypropylene in carbon nanotube conductive networks for improved electromagnetic interference shielding and flame retardation. *Adv. Funct. Mater.* **2021**, *23*, 2100024. [[CrossRef](#)]
22. Jia, L.C.; Yan, D.X.; Cui, C.H.; Jiang, X.; Ji, X.; Li, Z.M. Electrically conductive and electromagnetic interference shielding of polyethylene composites with devisable carbon nanotube networks. *J. Mater. Chem. C* **2015**, *3*, 9369–9378. [[CrossRef](#)]
23. Gao, C.; Lu, H.; Ni, H.; Chen, J. Structure, thermal conductive, dielectric and electrical insulating properties of UHMWPE/BN composites with a segregated structure. *J. Polym. Res.* **2017**, *25*, 6. [[CrossRef](#)]
24. Wang, Z.G.; Gong, F.; Yu, W.C.; Huang, Y.F.; Zhu, L.; Lei, J.; Xu, J.Z.; Li, Z.M. Synergetic enhancement of thermal conductivity by constructing hybrid conductive network in the segregated polymer composites. *Compos. Sci. Technol.* **2018**, *162*, 7–13. [[CrossRef](#)]
25. Zhou, H.; Deng, H.; Zhang, L.; Fu, Q. Significant enhancement of thermal conductivity in polymer composite via constructing macroscopic segregated filler networks. *ACS Appl. Mater. Int.* **2017**, *9*, 29071–29081. [[CrossRef](#)]
26. Liang, C.B.; Ruan, K.P.; Zhang, Y.L.; Gu, J.W. Multifunctional flexible electromagnetic interference shielding silver nanowires/cellulose films with excellent thermal management and joule heating performances. *ACS Appl. Mater. Int.* **2020**, *12*, 18023–18031. [[CrossRef](#)]
27. Zhao, B.; Zhao, C.X.; Li, R.S.; Hamidinejad, S.M.; Park, C.B. Flexible, ultrathin, and high-efficiency electromagnetic shielding properties of poly(vinylidene fluoride)/carbon composite films. *ACS Appl. Mater. Int.* **2017**, *9*, 20873–20884. [[CrossRef](#)]
28. Pawar, S.P.; Stephen, S.; Bose, S.; Mittal, V. Tailored electrical conductivity, electromagnetic shielding and thermal transport in polymeric blends with graphene sheets decorated with nickel nanoparticles. *Phys. Chem. Chem. Phys.* **2015**, *17*, 14922–14930. [[CrossRef](#)]
29. Ren, F.; Song, D.P.; Li, Z.; Jia, L.C.; Zhao, Y.C.; Yan, D.X.; Ren, P.G. Synergistic effect of graphene nanosheets and carbonyl iron-nickel alloy hybrid filler on electromagnetic interference shielding and thermal conductivity of cyanate ester composites. *J. Mater. Chem. C* **2018**, *6*, 1476–1486. [[CrossRef](#)]
30. Lin, S.F.; Ju, S.; Zhang, J.W.; Shi, G.; He, Y.L.; Jiang, D.Z. Ultrathin flexible graphene films with high thermal conductivity and excellent EMI shielding performance using large-sized graphene oxide flakes. *RSC Adv.* **2019**, *9*, 1419–1427. [[CrossRef](#)]
31. Liu, H.B.; Fu, R.L.; Su, X.Q.; Wu, B.Y.; Wang, H.; Xu, Y.; Liu, X.H. Electrical insulating Mxene/PDMS/BN composite with enhanced thermal conductivity for electromagnetic shielding application. *Compos. Commun.* **2021**, *23*, 100593. [[CrossRef](#)]
32. Raagulan, K.; Braveenth, R.; Kim, B.M.; Lim, K.J.; Lee, S.B.; Kim, M.; Chai, K.Y. An effective utilization of Mxene and its effect on electromagnetic interference shielding: Flexible, free-standing and thermally conductive composite from Mxene-PAT-Poly(P-Aminophenol)-Polyaniline co-polymer. *RSC Adv.* **2020**, *10*, 1613–1633. [[CrossRef](#)] [[PubMed](#)]

33. Yu, J.C.; Sundqvist, B.; Tonpheng, B.; Andersson, O. Thermal conductivity of highly crystallized polyethylene. *Polymer* **2014**, *55*, 195–200. [[CrossRef](#)]
34. Wang, J.; Hopmann, C.; Schmitz, M.; Hohlweck, T. Influence of measurement processes on pressure-specific volume-temperature relationships of semi-crystalline polymer: Polypropylene. *Polym. Test.* **2019**, *78*, 105992. [[CrossRef](#)]
35. Gere, D.; Czigany, T. Rheological and mechanical properties of recycled polyethylene films contaminated by biopolymer. *Waste Manag.* **2018**, *76*, 190–198. [[CrossRef](#)]
36. Xu, H.L.; Yin, X.W.; Li, X.L.; Li, M.H.; Liang, S.; Zhang, L.T.; Cheng, L.F. Lightweight Ti₂CT_x MXene/Poly(vinyl alcohol) composite foams for electromagnetic wave shielding with absorption-dominated feature. *ACS Appl. Mater. Int.* **2019**, *11*, 10198–10207. [[CrossRef](#)]
37. Cui, C.H.; Yan, D.X.; Pang, H.; Xu, X.; Jia, L.C.; Li, Z.M. Formation of a Segregated Electrically Conductive Network Structure in a Low-Melt-Viscosity Polymer for Highly Efficient Electromagnetic Interference Shielding. *ACS Sustain. Chem. Eng.* **2016**, *4*, 4137–4145. [[CrossRef](#)]
38. Chen, J.; Liao, X.; Xiao, W.; Yang, J.M.; Jiang, Q.Y.; Li, G.X. Facile and Green Method To Structure Ultralow-Threshold and Lightweight Polystyrene/MWCNT Composites with Segregated Conductive Networks for Efficient Electromagnetic Interference Shielding. *ACS Sustain. Chem. Eng.* **2019**, *7*, 9904–9915. [[CrossRef](#)]
39. Duan, H.J.; Xu, Y.D.; Yan, D.X.; Yang, Y.Q.; Zhao, G.Z.; Liu, Y.Q. Ultrahigh molecular weight polyethylene composites with segregated nickel conductive network for highly efficient electromagnetic interference shielding. *Mater. Lett.* **2017**, *209*, 353–356. [[CrossRef](#)]
40. Duan, H.J.; Zhu, H.X.; Yang, Y.Q.; Hou, T.T.; Zhao, G.Z.; Liu, Y.Q. Facile and economical fabrication of conductive polyamide 6 composites with segregated expanded graphite networks for efficient electromagnetic interference shielding. *J. Mater. Sci. Mater. Electron.* **2018**, *29*, 1058–1064. [[CrossRef](#)]
41. Fang, H.G.; Ye, W.J.; Yang, K.J.; Song, K.; Wei, H.B.; Ding, Y.S. Vitrimer chemistry enables epoxy nanocomposites with mechanical robustness and integrated conductive segregated structure for high performance electromagnetic interference shielding. *Compos. B Eng.* **2021**, *215*, 108782. [[CrossRef](#)]
42. Gao, C.Q.; Shi, Y.Q.; Chen, Y.J.; Zhu, S.C.; Feng, Y.Z.; Lv, Y.C.; Yang, F.Q.; Liu, M.H.; Shui, W. Constructing segregated polystyrene composites for excellent fire resistance and electromagnetic wave shielding. *J. Colloid Interface Sci.* **2022**, *606*, 1193–1204. [[CrossRef](#)] [[PubMed](#)]
43. Ge, C.B.A.; Wang, G.L.; Zhao, G.Q.; Wei, C.; Li, X.Y. Lightweight and flexible poly(ether-block-amide)/multiwalled carbon nanotube composites with porous structure and segregated conductive networks for electromagnetic shielding applications. *Compos. A Appl. Sci. Manuf.* **2021**, *144*, 106356. [[CrossRef](#)]
44. Jia, L.C.; Yan, D.X.; Jiang, X.; Pang, H.; Gao, J.F.; Ren, P.G.; Li, Z.M. Synergistic Effect of Graphite and Carbon Nanotubes on Improved Electromagnetic Interference Shielding Performance in Segregated Composites. *Ind. Eng. Chem. Res.* **2018**, *57*, 11929–11938. [[CrossRef](#)]
45. Li, T.; Zhao, G.; Zhang, L.; Wang, G.; Li, B.; Gong, J. Ultralow-threshold and efficient EMI shielding PMMA/MWCNTs composite foams with segregated conductive network and gradient cells. *Express Polym. Lett.* **2020**, *14*, 685–703. [[CrossRef](#)]
46. Sharif, F.; Arjmand, M.; Moud, A.A.; Sundararaj, U.; Roberts, E.P.L. Segregated Hybrid Poly(methyl methacrylate)/Graphene/Magnetite Nanocomposites for Electromagnetic Interference Shielding. *ACS Appl. Mater. Interfaces* **2017**, *9*, 14171–14179. [[CrossRef](#)]
47. Tang, X.H.; Tang, Y.; Wang, Y.; Weng, Y.X.; Wang, M. Interfacial metallization in segregated poly(lactic acid)/poly(ϵ -caprolactone)/multi-walled carbon nanotubes composites for enhancing electromagnetic interference shielding. *Compos. A Appl. Sci. Manuf.* **2020**, *139*, 106116. [[CrossRef](#)]
48. Wang, G.L.; Wang, L.; Mark, L.H.; Shaayegan, V.; Wang, G.Z.; Li, H.P.; Zhao, G.Q.; Park, C.B. Ultralow-Threshold and Lightweight Biodegradable Porous PLA/MWCNT with Segregated Conductive Networks for High-Performance Thermal Insulation and Electromagnetic Interference Shielding Applications. *ACS Appl. Mater. Interfaces* **2018**, *10*, 1195–1203. [[CrossRef](#)]
49. Wang, H.; Zheng, K.; Zhang, X.; Du, T.X.; Xiao, C.; Ding, X.; Bao, C.; Chen, L.; Tian, X.Y. Segregated poly(vinylidene fluoride)/MWCNTs composites for high-performance electromagnetic interference shielding. *Compos. A Appl. Sci. Manuf.* **2016**, *90*, 606–613. [[CrossRef](#)]
50. Wang, T.; Kong, W.W.; Yu, W.C.; Gao, J.F.; Dai, K.; Yan, D.X.; Li, Z.M. A Healable and Mechanically Enhanced Composite with Segregated Conductive Network Structure for High-Efficient Electromagnetic Interference Shielding. *Nano-Micro Lett.* **2021**, *13*, 1–14. [[CrossRef](#)]
51. Wang, T.; Yu, W.C.; Sun, W.J.; Jia, L.C.; Gao, J.F.; Tang, J.H.; Su, H.J.; Yan, D.X.; Li, Z.M. Healable polyurethane/carbon nanotube composite with segregated structure for efficient electromagnetic interference shielding. *Compos. Sci. Technol.* **2020**, *200*, 108446. [[CrossRef](#)]
52. Wu, H.Y.; Jia, L.C.; Yan, D.X.; Gao, J.F.; Zhang, X.P.; Ren, P.G.; Li, Z.M. Simultaneously improved electromagnetic interference shielding and mechanical performance of segregated carbon nanotube/polypropylene composite via solid phase molding. *Compos. Sci. Technol.* **2018**, *156*, 87–94. [[CrossRef](#)]
53. Yan, D.X.; Pang, H.; Xu, L.; Bao, Y.; Ren, P.G.; Lei, J.; Li, Z.M. Electromagnetic interference shielding of segregated polymer composite with an ultralow loading of in situ thermally reduced graphene oxide. *Nanotechnology* **2014**, *25*, 145705. [[CrossRef](#)] [[PubMed](#)]

54. Yu, W.C.; Wang, T.; Zhang, G.Q.; Wang, Z.G.; Yin, H.M.; Yan, D.X.; Xu, J.Z.; Li, Z.M. Largely enhanced mechanical property of segregated carbon nanotube/poly (vinylidene fluoride) composites with high electromagnetic interference shielding performance. *Compos. Sci. Technol.* **2018**, *167*, 260–267. [[CrossRef](#)]
55. Yu, W.C.; Zhang, G.Q.; Liu, Y.H.; Xu, L.; Yan, D.X.; Huang, H.D.; Tang, J.H.; Xu, J.Z.; Li, Z.M. Selective electromagnetic interference shielding performance and superior mechanical strength of conductive polymer composites with oriented segregated conductive networks. *Chem. Eng. J.* **2019**, *373*, 556–564. [[CrossRef](#)]
56. Yuan, D.; Guo, H.C.; Ke, K.; Manas-Zloczower, I. Recyclable conductive epoxy composites with segregated filler network structure for EMI shielding and strain sensing. *Compos. A Appl. Sci. Manuf.* **2020**, *132*, 105837. [[CrossRef](#)]
57. Zhang, K.; Li, G.H.; Feng, L.M.; Wang, N.; Guo, J.; Sun, K.; Yu, K.X.; Zeng, J.B.; Li, T.X.; Guo, Z.H.; et al. Ultralow percolation threshold and enhanced electromagnetic interference shielding in poly(L-lactide)/multi-walled carbon nanotube nanocomposites with electrically conductive segregated networks. *J. Mater. Chem. C* **2017**, *5*, 9359–9369. [[CrossRef](#)]
58. Zhang, K.; Yu, H.O.; Yu, K.X.; Gao, Y.; Wang, M.; Li, J.; Guo, S.Y. A facile approach to constructing efficiently segregated conductive networks in poly(lactic acid)/silver nanocomposites via silver plating on microfibers for electromagnetic interference shielding. *Compos. Sci. Technol.* **2018**, *156*, 136–143. [[CrossRef](#)]
59. Zhang, X.P.; Jia, L.C.; Zhang, G.; Yan, D.X.; Li, Z.M. A highly efficient and heat-resistant electromagnetic interference shielding carbon nanotube/poly(phenylene sulfide) composite via sinter molding. *J. Mater. Chem. C* **2018**, *6*, 10760–10766. [[CrossRef](#)]
60. Chaudhary, A.; Kumar, R.; Dhakate, S.R.; Kumari, S. Scalable development of a multi-phase thermal management system with superior EMI shielding properties. *Compos. B Eng.* **2019**, *158*, 206–217. [[CrossRef](#)]
61. Chaudhary, A.; Teotia, S.; Kumar, R.; Gupta, V.; Dhakate, S.R.; Kumari, S. Multi-component framework derived SiC composite paper to support efficient thermal transport and high EMI shielding performance. *Compos. B Eng.* **2019**, *176*, 107123. [[CrossRef](#)]
62. Guo, Y.Q.; Pan, L.L.; Yang, X.T.; Ruan, K.P.; Han, Y.X.; Kong, J.; Gu, J.W. Simultaneous improvement of thermal conductivities and electromagnetic interference shielding performances in polystyrene composites via constructing interconnection oriented networks based on electrospinning technology. *Compos. A Appl. Sci. Manuf.* **2019**, *124*, 105484. [[CrossRef](#)]
63. Jin, X.X.; Wang, J.F.; Dai, L.Z.; Liu, X.Y.; Li, L.; Yang, Y.Y.; Cao, Y.X.; Wang, W.J.; Wu, H.; Guo, S.Y. Flame-retardant poly(vinyl alcohol)/MXene multilayered films with outstanding electromagnetic interference shielding and thermal conductive performances. *Chem. Eng. J.* **2020**, *380*, 122475. [[CrossRef](#)]
64. Kim, J.M.; Lee, Y.; Jang, M.G.; Han, C.; Kim, W.N. Electrical conductivity and EMI shielding effectiveness of polyurethane foam-conductive filler composites. *J. Appl. Polym. Sci.* **2017**, *134*, 44373. [[CrossRef](#)]
65. Li, J.C.; Zhao, X.Y.; Wu, W.J.; Ji, X.W.; Lu, Y.L.; Zhang, L.Q. Bubble-templated rGO-graphene nanoplatelet foams encapsulated in silicon rubber for electromagnetic interference shielding and high thermal conductivity. *Chem. Eng. J.* **2021**, *415*, 129054. [[CrossRef](#)]
66. Li, J.P.; Qi, S.H.; Zhang, M.Y.; Wang, Z.F. Thermal conductivity and electromagnetic shielding effectiveness of composites based on Ag-plating carbon fiber and epoxy. *J. Appl. Polym. Sci.* **2015**, *132*, 42306. [[CrossRef](#)]
67. Liang, C.B.; Qiu, H.; Han, Y.Y.; Gu, H.B.; Song, P.; Wang, L.; Kong, J.; Cao, D.P.; Gu, J.W. Superior electromagnetic interference shielding 3D graphene nanoplatelets/reduced graphene oxide foam/epoxy nanocomposites with high thermal conductivity. *J. Mater. Chem. C* **2019**, *7*, 2725–2733. [[CrossRef](#)]
68. Liang, C.Y.; Hamidinejad, M.; Ma, L.; Wang, Z.J.; Park, C.B. Lightweight and flexible graphene/SiC-nanowires/poly(vinylidene fluoride) composites for electromagnetic interference shielding and thermal management. *Carbon* **2020**, *156*, 58–66. [[CrossRef](#)]
69. Liang, L.Y.; Xu, P.H.; Wang, Y.F.; Shang, Y.; Ma, J.M.; Su, F.M.; Feng, Y.Z.; He, C.G.; Wang, Y.M.; Liu, C.T. Flexible polyvinylidene fluoride film with alternating oriented graphene/Ni nanochains for electromagnetic interference shielding and thermal management. *Chem. Eng. J.* **2020**, *395*, 125209. [[CrossRef](#)]
70. Liu, C.; Wu, W.; Wang, Y.; Wang, Z.Y.; Chen, Q.M. Silver-coated thermoplastic polyurethane hybrid granules for dual-functional elastomer composites with exceptional thermal conductive and electromagnetic interference shielding performances. *Compos. Commun.* **2021**, *25*, 100719. [[CrossRef](#)]
71. Shen, Z.M.; Feng, J.C. Preparation of Thermally Conductive Polymer Composites with Good Electromagnetic Interference Shielding Efficiency Based on Natural Wood-Derived Carbon Scaffolds. *ACS Sustain. Chem. Eng.* **2019**, *7*, 6259–6266. [[CrossRef](#)]
72. Shi, H.G.; Zhao, H.B.; Liu, B.W.; Wang, Y.Z. Multifunctional Flame-Retardant Melamine-Based Hybrid Foam for Infrared Stealth, Thermal Insulation, and Electromagnetic Interference Shielding. *ACS Appl. Mater. Interfaces* **2021**, *13*, 26505–26514. [[CrossRef](#)] [[PubMed](#)]
73. Song, P.; Liu, B.; Liang, C.B.; Ruan, K.P.; Qiu, H.; Ma, Z.L.; Guo, Y.Q.; Gu, J.W. Lightweight, Flexible Cellulose-Derived Carbon Aerogel@Reduced Graphene Oxide/PDMS Composites with Outstanding EMI Shielding Performances and Excellent Thermal Conductivities. *Nano-Micro Lett.* **2021**, *13*, 1–17. [[CrossRef](#)] [[PubMed](#)]
74. Wang, L.; Qiu, H.; Liang, C.B.; Song, P.; Han, Y.X.; Han, Y.X.; Gu, J.W.; Kong, J.; Pan, D.; Guo, Z.H. Electromagnetic interference shielding MWCNT-Fe₃O₄@Ag/epoxy nanocomposites with satisfactory thermal conductivity and high thermal stability. *Carbon* **2019**, *141*, 506–514. [[CrossRef](#)]
75. Wang, Y.; Wang, W.; Xu, R.; Zhu, M.F.; Yu, D. Flexible, durable and thermal conducting thiol-modified rGO-WPU/cotton fabric for robust electromagnetic interference shielding. *Chem. Eng. J.* **2019**, *360*, 817–828. [[CrossRef](#)]

76. Wei, L.F.; Ma, J.Z.; Zhang, W.B.; Bai, S.L.; Ren, Y.N.; Zhang, L.; Wu, Y.K.; Qin, J.B. pH triggered hydrogen bonding for preparing mechanically strong, electromagnetic interference shielding and thermally conductive waterborne polymer/graphene@polydopamine composites. *Carbon* **2021**, *181*, 212–224. [[CrossRef](#)]
77. Yang, X.T.; Fan, S.G.; Li, Y.; Guo, Y.Q.; Li, Y.G.; Ruan, K.P.; Zhang, S.M.; Zhang, J.L.; Kong, J.; Gu, J.W. Synchronously improved electromagnetic interference shielding and thermal conductivity for epoxy nanocomposites by constructing 3D copper nanowires/thermally annealed graphene aerogel framework. *Compos. A Appl. Sci. Manuf.* **2020**, *128*, 105670. [[CrossRef](#)]
78. Zhan, Y.H.; Cheng, Y.; Yan, N.; Li, Y.C.; Meng, Y.Y.; Zhang, C.M.; Chen, Z.M.; Xia, H.S. Lightweight and self-healing carbon nanotube/acrylic copolymer foams: Toward the simultaneous enhancement of electromagnetic interference shielding and thermal insulation. *Chem. Eng. J.* **2021**, *417*, 129339. [[CrossRef](#)]
79. Zhang, H.M.; Zhang, G.C.; Gao, Q.; Tang, M.; Ma, Z.L.; Qin, J.B.; Wang, M.Y.; Kim, J.K. Multifunctional microcellular PVDF/Ni-chains composite foams with enhanced electromagnetic interference shielding and superior thermal insulation performance. *Chem. Eng. J.* **2020**, *379*, 122304. [[CrossRef](#)]
80. Zhou, B.; Li, Q.T.; Xu, P.H.; Feng, Y.Z.; Ma, J.M.; Liu, C.T.; Shen, C.Y. An asymmetric sandwich structural cellulose-based film with self-supported MXene and AgNW layers for flexible electromagnetic interference shielding and thermal management. *Nanoscale* **2021**, *13*, 2378–2388. [[CrossRef](#)]
81. Zong, Z.; Ren, F.; Guo, Z.Z.; Lu, Z.X.; Jin, Y.L.; Zhao, Y.C.; Ren, P.G. Dual-functional carbonized loofah@GNSs-CNTs reinforced by cyanate ester composite with highly efficient electromagnetic interference shielding and thermal management. *Compos. B Eng.* **2021**, *223*, 109132. [[CrossRef](#)]
82. Yuan, Y.; Liu, L.Y.; Yang, M.L.; Zhang, T.L.; Xu, F.; Lin, Z.S.; Ding, Y.J.; Wang, C.H.; Li, J.J.; Yin, W.L.; et al. Lightweight, thermally insulating and stiff carbon honeycomb-induced graphene composite foams with a horizontal laminated structure for electromagnetic interference shielding. *Carbon* **2017**, *123*, 223–232. [[CrossRef](#)]
83. Guo, Y.L.; Zhang, R.Z.; Wu, K.; Chen, F.; Fu, Q. Preparation of Nylon MXD6/EG/CNTs Ternary Composites with Excellent Thermal Conductivity and Electromagnetic Interference Shielding Effectiveness. *Chin. J. Polym. Sci.* **2017**, *35*, 1497–1507. [[CrossRef](#)]
84. Li, Y.; Xu, F.; Lin, Z.S.; Sun, X.X.; Peng, Q.Y.; Yuan, Y.; Wang, S.S.; Yang, Z.Y.; He, X.D.; Li, Y.B. Electrically and thermally conductive underwater acoustically absorptive graphene/rubber nanocomposites for multifunctional applications. *Nanoscale* **2017**, *9*, 14476–14485. [[CrossRef](#)]
85. Liu, P.S.; Qing, H.B.; Hou, H.L.; Wang, Y.Q.; Zhang, Y.L. EMI shielding and thermal conductivity of a high porosity reticular titanium foam. *Mater. Des.* **2016**, *92*, 823–828. [[CrossRef](#)]